Expanding subatmospheric plasmas used for plasma deposition

High-Temp. Dust Laden Jets, pp. 329-348 (1989)
Solonenko and Fedorchenko (Eds)

Expanding Subatmospheric Plasmas used for Plasma Deposition

D.C. Schram, G.M.W. Kroesen, and J.C.M. de Haas+

Department of Physics, Eindhoven University of Technology, P.O. Box 513, 5600 MB Eindhoven, The Netherlands
+present address: JET Joint Undertaking, Abingdon, U.K.

ABSTRACT

In this paper a new method of plasma deposition is discussed which is used to produce amorphous hydrogenated carbon layers. The method is in the general set up quite similar to the ones used for low pressure plasma spraying. The power is lower and the growth of the layer, which is fast compared to traditional deposition methods, is still substantially smaller than is achievable with plasma spraying. At the other hand thin layers with high quality can be produced. The apparatus and the diagnostics are discussed in section 2, the model in section 3, and the results of the model are compared with experimental data in section 4. Finally, conclusions are given in section 5.

1. INTRODUCTION

In the conference of "High Temperature Dust–Laden Jets in the Processes of Treatment of Powder Materials" the discussion of a deposition method with atomic (or molecular) particles is an exception. Still the similarity of this new method of plasma deposition with low pressure plasma spraying makes a discussion attractive. It serves also to demonstrate the usefulness of (sub)atmospheric plasmas for plasma surface modification in view of the then achievable favourable material and energy efficiencies. The latter are essential to achieve high deposition rates and therewith a low cost process.

Plasma enhanced chemical vapour deposition is traditionally developed from the chemical vapour deposition. It was argued that in gas discharges higher (electron) temperatures were achievable and therewith relatively high radical densities at low pressures. However, plasmas and in particular gas discharges with a low ionization degree are non–equilibrium systems. As a consequence, existence demands related to mass and energy balances interrelate the plasma parameters as electron density and temperature with plasma conditions as dimensions, pressure and power density. This has as a consequence that with

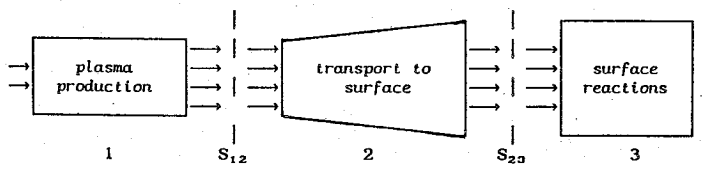

Figure 1. Schematic set–up of the plasma deposition process.

acceptable power flux (typically 1 W/cm^2) at the substrate the deposition rate is limited [1] to typically 1 nm/s. The principle limitation arises from the fact that the plasma treatment is performed in the same volume where the plasma is produced, therewith coupling the existence demands with deposition conditions.

In the here to be discussed method the production of the plasma is geometrically separated from the plasma treatment as indicated schematically in Fig. 1. Since the power loading of the substrate is limited to the power flux in the plasma beam, significantly higher power levels can be used in the production section without leading to excessive power loading of the substrate. Also the conditions of plasma production can be separately optimized; then (sub)atmospheric arcs with a small diameter are the best approach as they are very energy efficient and can handle a large throughput. The plasma thus formed has also a high heavy particle temperature and as the expansion into the vacuum chamber will be supersonic, large velocities are obtained. With the high densities large fluences are achievable with corresponding large deposition rates. The third advantage is that nearby total dissociation is achieved; also ionization in these plasmas, which are not too far from equilibrium, is preferred for the ion with the lowest ionization potential. This is usually the atom to be deposited, in our case carbon. In this way the emanating plasma beam is enriched with the to be deposited ions and good material efficiencies can be obtained. Finally, the plasma beam remains restricted in dimensions, therewith permitting observation through observation windows. At the same time this also points to the possibility of good material efficiencies. Still at the substrate only small potentials are developed as the electron density is still relatively large. Therefore, at the substrate it is mainly the ionization energy which becomes available in the deposition process.

Returning to the matter of the relation between this deposition process and

low pressure plasma spraying we can remark the following. The experimental arrangement is not too far different from a plasma spraying gun with an extended segmented anode section. The differences are in the larger length, smaller radial dimensions, lower power, but significantly stronger pumping speed in the vacuum section. The study of the physics of the flowing plasma is essentially the same problem for both approaches.

2. DESCRIPTION OF APPARATUS AND DIAGNOSTICS

2.1. Description

As has been argued in the introduction the main principle of the new deposition scheme is to separate the production of the plasma from the plasma treatment. In this section the reactor shown in Fig. 2 will be described in more

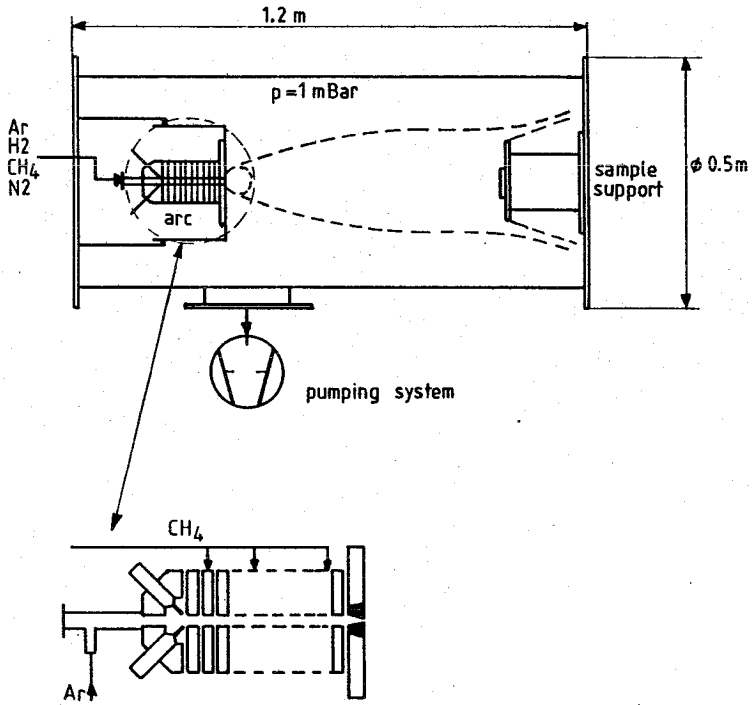

Figure 2a. Outline of the plasma deposition reactor used in the present experiments. Figure 2b. Schematic view of the cascaded arc.

detail and we will start with the production section.

The plasma is produced in a subatmospheric cascaded arc. These arcs introduced by Maecker in 1956 [2] pair a very efficient ionization with good energy efficiency. These arcs have been studied in great detail mainly for spectroscopic research and to establish quantitatively the small deviations from local thermal equilibrium (LTE). In the present reactor the plasma is flowing which, of course, will alter the behaviour of the plasma. Even though the plasma is still close to LTE the deviations will be larger in view of the now appearing convective losses [3]. The construction of the cascaded arc is optimized for use in deposition processes [4]. Three cathodes are used of 1 mm diameter thoriated tungsten or 2 mm for currents larger than 30 A per cathode. The cathodes are at the high pressure side of the discharge where argon is used as carrier pas. The wear is very small; in the order of 10^{-10} g/C. With the high deposition rates this leads to impurity levels in the deposited layer which are substantially smaller than 0.1 ppm. In fact, metal impurities could not be detected with SIMS (detection limit 1 ppm).

The cascaded arc is made up of 10 cascaded plates of 5 mm thickness which are water–cooled. They are isolated from each other by isolation rings; these rings are shielded from the plasma by smaller rings of teflon. The diameter of the plasma channel is 4 mm. Close to the anode methane or acethylene is introduced in the arc. The anode is a copper insert and serves at the same time as nozzle. It is mounted in a water–cooled flange, which connects the cascade arc section with the vacuum chamber in which the plasma expands and is accelerated to the substrate. After the nozzle the high density plasma expands in the vacuum chamber. The latter has a length of 1.2 m and a diameter of 0.5 m, cf. Fig. 2. Through several windows the plasma can be observed. The substrate holder is mounted on a movable support holder, which can be moved axially. The normal position is at 0.8 m from the anode nozzle. An oil diffusion pump is used to obtain a background pressure below 10^{-6} mbar. During deposition the large flows are pumped by two rootsblowers in series (2600 m^3/hr and 400 m^3/hr). They are pumped by a 100 m^3/hr mechanical rotary piston pump. Typical pressure in the vacuum chamber during deposition is 1 mbar. In table I experimental conditions are summarized.

The substrate support can be biased with respect to the nozzle–anode which is grounded.

Table 1. Summary of experimental conditions

cascade arc		**vacuum chamber**	
– current	20–70 A	– pressure	0.1–10 mbar
– voltage	50–150 V	– substrate bias voltage	0–200 V
– pressure	0.1–2 bar		
– argon flow	100 scc/s		
– methane flow	1 scc/s		

2.1. Diagnostics

High pressure cascade arc section

In the cascade plates glass fibres are inserted through which the plasma in the arc can be observed. With this system first the broadening of H_β Balmer line is measured to obtain the electron density according to

$$n_e = C\,\Delta\lambda^{3/2}\,, \tag{1}$$

in which $\Delta\lambda$ is the full width in nm at half maximum of the Lorentz part of the line and C is a constant nearly independent of temperature with a magnitude for $T_e \sim 1$ eV;

$$C = 1.2\ 10^{22}\ \mathrm{m^{-3}\ nm^{-3/2}}\,. \tag{2}$$

In the employed range of electron density the contributions of other broadening mechanisms as resonance broadening, van der Waals broadening etc. are negligible small.

Secondly, line to continuum ratio is measured to determine the electron temperature. The observed line Ar II 480.6 nm is from the 4p level of the ionized argon system. The emissivities of the line and of the continuum are:

$$\epsilon_l = n_p^{\,II}\, A_{pq}\, h\nu\, P_l/4\pi \tag{3}$$

$$\epsilon_c = C_l \frac{n_e^{\,2}}{\lambda^2\sqrt{T_e}} \{ G_l[\lambda, T_e] + [1 - \exp(-\frac{h\nu}{kT_e})]\xi_{fb} \}\,, \tag{4}$$

in which the following symbols are used:

n_p^{II} = the density of the observed 4p level
A_{pq} = the transition probability of the observed line
P_l = normalized profile
C_l = constant ($1.63\ 10^{-43}\ Wm^4\ K^{\frac{1}{2}}\ sr^{-1}$)
G_l = Gaunt factor ($\simeq 1.2 \exp[-h\nu/kT_e]$ at $\lambda = 420.0$ nm)
ξ_{fb} = Biberman fb factor ($\simeq 1.55$ at $\lambda = 420.0$ nm)
T_e = electron temperature in K.

In the expression for continuum emission we have assumed the presence of singly charged ions only. The population density of the $4p^{II}$ level can be related to the argon II ground level density by:

$$n_{4p}{}^{II}/g_{4p} = b_{4p}{}^{+}\, n_1{}^{+}/g_1 \exp\left[-\frac{E_{4p}{}^{II}}{kT_e}\right] \tag{5}$$

in which n^+ is the density of the ion ground levels and g_{4p} and g_1 are the statistical weights of the $4p^{II}$ level and the two ground states of Ar^+; $E4p^{II}$ is the excitation energy of the $4p^{II}$ level and $b_{4p}{}^+$ is the so–called overpopulation factor. A full collisional radiative model [5], which has been tested extensively for the electron density and temperature ranges of 10^{19}–$10^{21}/m^3$ and 2–5 eV, respectively, has been used to obtain a good estimate [6] for b_{4p} for the present conditions:

$$b_{4p}{}^{+} \sim 0.3\ (n_e \sim 10^{22}/m^3,\ T_e \sim 1\ eV)\ .$$

Furthermore, a provision has been made in the cascade plates to measure the axial dependence of the pressure. To obtain the resistivity of the plasma and the electron temperature from the potential drop, also the potentials of the cascade plates can be measured.

In the low pressure section the expansion of the plasma is observed by several optical techniques. In Fig. 3 the optical arrangement is depicted. The plasma can be observed perpendicularly with the axis of the chamber and under an angle of 60^0. The sensitivity pattern of the latter arrangement is shown in Fig. 4. With that arrangement the axial velocity component is

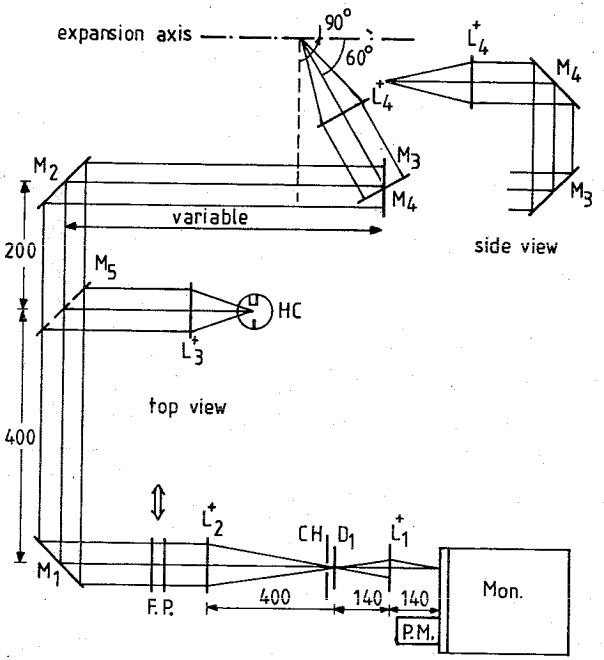

Figure 3. The optical system. Lenses L_1–L_4, Mirrors M_1–M_5, Diafragma D_1, Monochromator MON, Photomultiplier PM, Fabry–Pérot interferometer FP, Chopper CH, low pressure reference source HC. All indicated distances are in mm.

measured by determining the Doppler shift of an argon line, by comparison with a calibration source. In Fig. 5 a measurement is shown. The optical arrangement is essentially made up by a monochromator and a Fabry–Pérot interferometer. Perpendicularly the broadening of the line is observed, which yields the neutral particle temperature from Doppler broadening. Again the H_β broadening is used to obtain the electron density. It should be noted that the expression in eq. (1) is, strictly speaking, only applicable at higher densities. However, comparisons with higher Balmer lines in an ICP with comparable densities show that the expression is still valid at those lower densities [7].

The deposition rate follows from ellipsometry [8]. In this method the complex ratio of the reflectence of the two signals with the two orthogonal polarizations is measured. From this ratio the so–called phase angles Ψ,Δ can be obtained and from these the thickness δ, the index of refraction n and the absorption coefficient α are calculated. As this method is employed *in situ*,

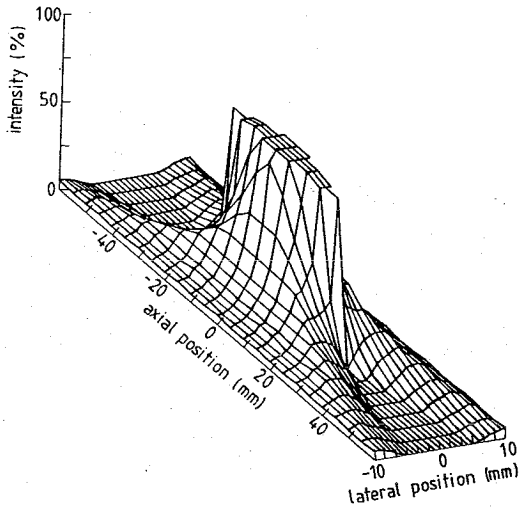

Figure 4. The relative intensity transmitted by the optical system as a function of the position in the detection volume. Basically, the volume consists of a cylinder with a length of 40 mm and a diameter of 4 mm.

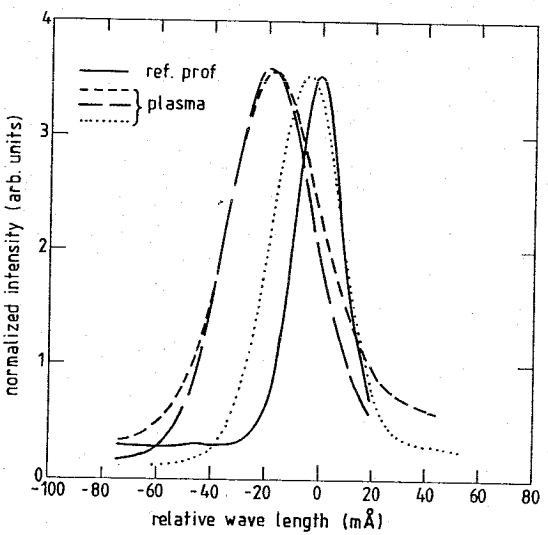

Figure 5. Shift of the argon neutral line 420.0 nm, measured at several axial positions, as compared to the reference line.

———— the reference line
– – – – spectral line at z = 30 mm
—— —— spectral line at z = 20 mm
. . . . spectral line at z = 60 mm

these three quantities follow in an unique way from the measurements. This is achieved by reproducing the trajectories in the Ψ,Δ plane, assuming the correct values for the three quantities δ, n and α in a minimization procedure. The layers can be further characterized by an *ex situ* spectroscopic ellipsometer. Here the index of refraction and absorption coefficient are determined as a function of photon energy in the range of 200–700 nm. In this way the bandgap behaviour can be studied and the bandgap energies can be determined.

3. MODEL CALCULATIONS

In the model calculations the two elements of the deposition process, i.e., the production of the plasma in the cascade arc, the expansion through the nozzle, the shock and the subsequent expanding flow are calculated. The results on the cascade arc [9] with the injection of methane in the last cascade section serve as starting point for the calculation of the expansion process in the vacuum chamber.

The evolution of densities, flow velocity and temperature is followed by solving the conservation laws for mass, momentum and energy. In the model [10] we integrate over the plasma cross–section so essentially a one–dimensional model is considered. The mass conservation leads to:

$$\nabla\cdot(n_h\,\underline{u}) = 0 \text{ or } \nabla\cdot\underline{u} = \underline{u}\,\frac{\nabla n_h}{n_h}, \tag{6}$$

in which $\underline{u}$ is the plasma flow velocity and $n_h = n_o + n_i$ is the heavy particle number density, i.e., the sum of all neutral and ion species in the plasma. The electron density then follows from the mass conservation of electrons taking into account that $\nabla\cdot\underline{j} = 0$:

$$\frac{\partial n_e}{\partial x} = \frac{1}{u}[k_1{}^+ n_e(n_{ar}-n_{ar}{}^s) - n_e{}^2 k_{+1}] + n_e[\frac{1}{p}\frac{\partial p}{\partial x} - \frac{1}{T_h}\frac{\partial T_h}{\partial x}]. \tag{7}$$

In the equation $K_1{}^+$ is the total ionization rate, i.e., both by direct and stepwise processes; $n_{ar}-n_{ar}{}^s$ is the argon atom density above the Saha density $n_{ar}{}^s$ and K_{+1} is the radiative recombination rate. In deriving eq. (7), the mass conservation of heavy particles, eq. (6) has been used. The $\nabla n_h/n_h$ has been

rewritten as $\frac{\nabla p_h}{p_h} - \frac{\nabla T_h}{T_h}$. As the results will show the gradient of the heavy particle pressure ∇p_h is nearly equal to the gradient of the total pressure ∇p in the axial direction:

$$p = p_e + p_h \simeq p_h \tag{8}$$

$$\frac{\partial p}{\partial x} = \frac{\partial p_e}{\partial x} + \frac{\partial p_h}{\partial x} \simeq \frac{\partial p_h}{\partial x} . \tag{9}$$

First $p_e/p_h << 1$, but also the electron pressure is nearly x–independent. The ionization and dissociation of C–H fragments of the methane, injected in the last section of the cascade arc is followed by a set of production equations:

$$\frac{\partial n_{C/H}}{\partial x} = \frac{1}{u}[\text{production C/H–destruction C/H}] + n_{C/H}\left(\frac{1}{T_h}\frac{\partial T_h}{\partial x} + \frac{1}{p}\frac{\partial p}{\partial x}\right), \tag{10}$$

in which $n_{C/H}$ stands for the number density of any C/H radical or ion.

The flow velocity $\underline{u}$ is obtained from the momentum conservation for the heavy particles

$$\rho(\underline{u}\cdot\nabla)\underline{u} + \nabla p + \nabla : \underline{\underline{\pi}} = 0 , \tag{11}$$

which integrated over the cross section can be rewritten in a one–dimensional form

$$\rho u \frac{\partial u}{\partial x} + \frac{\partial p}{\partial x} = -\frac{1}{2}\rho u^2 \frac{f}{D} . \tag{12}$$

Here, ρ stands for the mass density, f is the wall friction factor and D is the diameter of the arc channel. Separate measurements have shown that the friction factor f follows approximately the ideal laminar case (cf. Fig. 6):

$$f = \frac{64}{R_d} = \frac{64}{\rho u D}\eta , \tag{13}$$

in which η is the plasma viscosity coefficient, as shown in Fig. 7 [11].

The evolution of electron and heavy particle temperatures is followed with the energy balances. For details we refer to reference [10]. The total enthalpy h

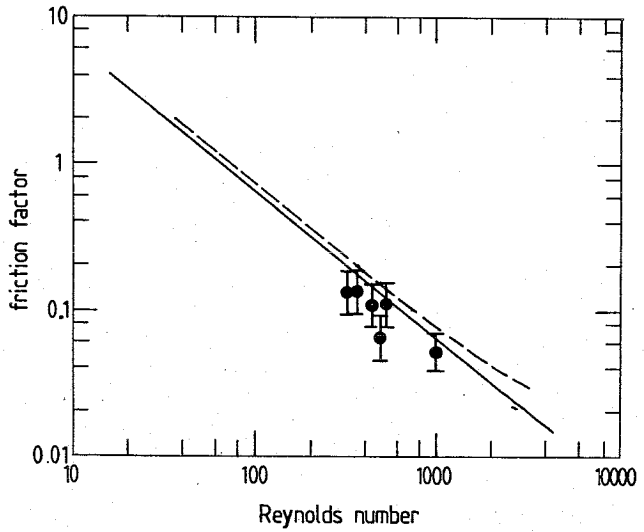

Figure 6. The wall friction factor f plotted versus the Reynolds number. The full curve corresponds to the ideal laminar case ($f=64/R_d$) and the dashed curve represents the measurements without a plasma being present in the arc channel (room temperature). The points are obtained from measurements at the beginning and at the end of the channel for a number of discharge conditions.

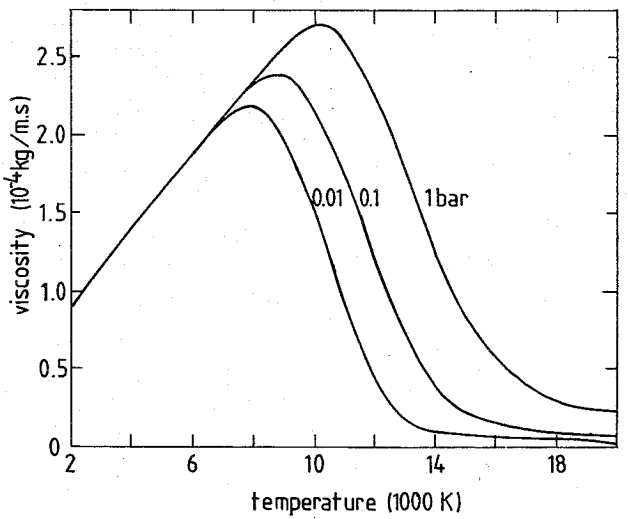

Figure 7. Viscosity of an LTE argon plasma as a function of temperature for three different pressures. The values are taken from Vargaftik [11].

follows then from

$$u \frac{\partial h}{\partial x} + u^2 \frac{\partial u}{\partial x} = q \,, \tag{14}$$

in which q is the energy source term.

For the plasma in the expansion zone in the low pressure section, separate equations for electron temperature and heavy particle temperature are used.

4. RESULTS AND COMPARISON WITH MODEL CALCULATION

4.1. High pressure arc section

In Fig. 8a the calculated axial pressure dependence is shown. In Fig. 8b the calculated heavy particle temperature is depicted together with measured values of the electron temperature. It can be concluded that the electron temperature is nearly constant; dependent on the argon flow it takes a small distance for the heavy particle temperature to become equal to the electron temperature.

In Fig. 9 the measured electron density is compared with the results of the model. A good agreement is observed; only for low flows and large z the measured electron density is lower than predicted. This discrepancy is very likely due to the neglect of sidewards diffusion, which for low flows leads to additional losses. Note, that the electron pressure remains approximately constant; this gives even more reason to ignore the variation of electron pressure in eqs. (7) and (10).

In Fig. 10 the carbon ion density evolution is shown; at large fluxes it takes apparently quite a distance for the carbon atoms to become ionized. Note that, according to the model, carbon ion fluences of $N_{C^+} = 10^{19}$/s can be obtained. If this fluence at the position of the substrate (see section 4.2) has a cross section of 100 cm^2, fluxes of 10^{21} ions/m^2 can apparently be obtained with his method. This is a factor of 100 higher than in conventional methods.

4.2. The expansion

A few cms behind the exit nozzle the plasma accelerates and forms a shock.

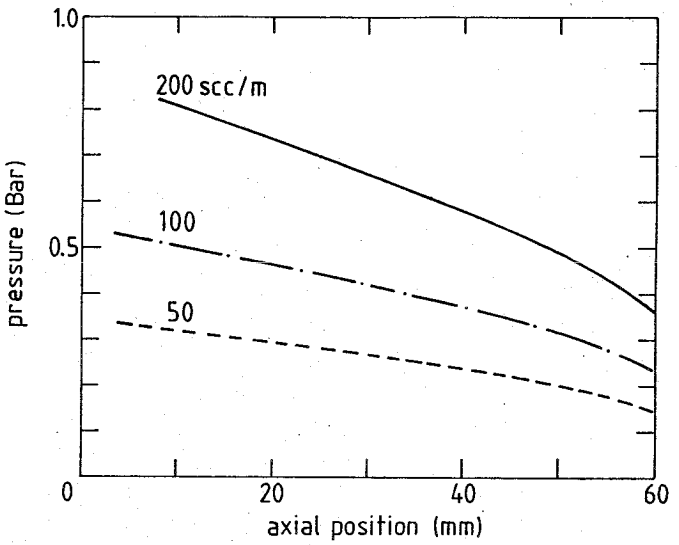

Figure 8a. Plasma pressure as a function of axial position in the arc channel. Parameter is the argon flow (50, 100 and 200 scc/s); 1 scc/s is defined as 1 cc/s at 1 bar and 273 K. The axial position is defined zero at the location of the cathodes at the beginning of the arc. The length of the channel (ending in the anode nozzle) is 60 mm.

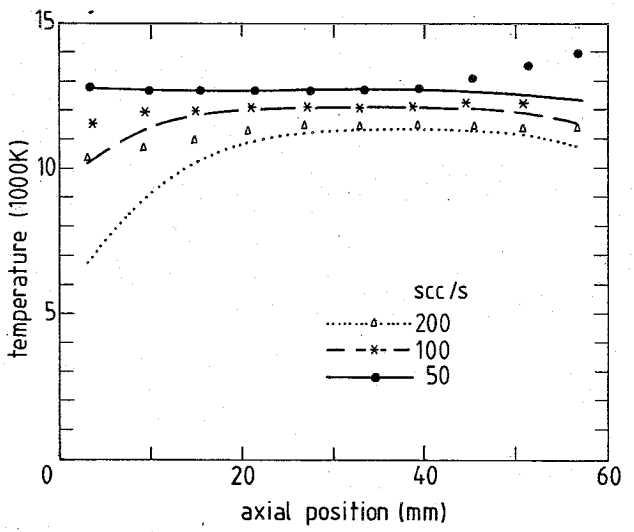

Figure 8b. The various temperatures as a function of axial position. Parameter is the argon flow (50, 100 and 200 scc/s). The points represent the values of the **electron** temperature as measured with line–continuum ratio, whereas the curves correspond to the calculations for the **gas** temperature.

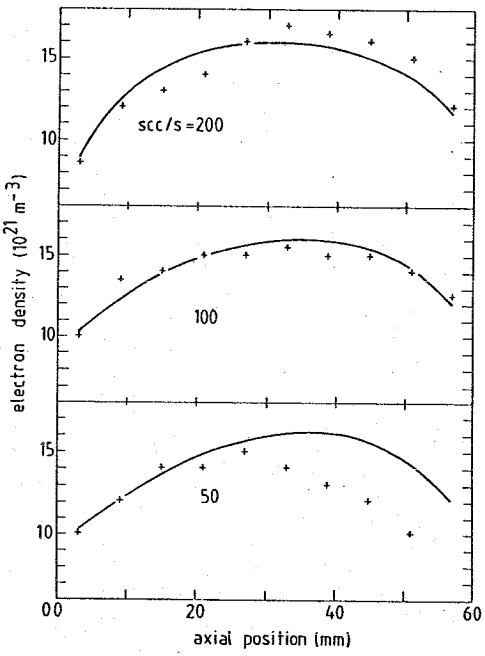

Figure 9. Comparison of the measured (points) and calculated (curves) axial profiles of the electron density in the arc channel for three values of the argon flow (50, 100 and 200 scc/s).

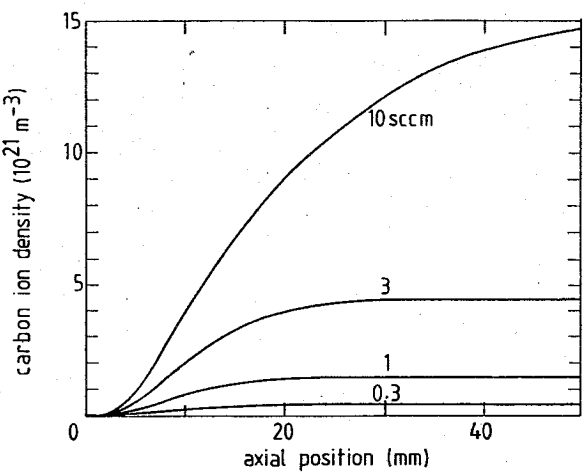

Figure 10. Evolution of the carbon ion density following injection of methane. Parameter is the methane flow (0.3, 1, 3 and 10 scc/s).

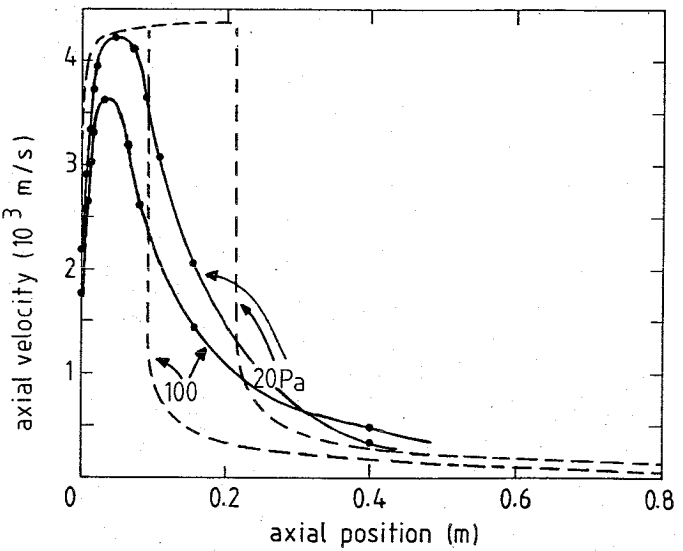

Figure 11. Comparison of measured and calculated axial profiles of the plasma velocity in the supersonic expansion followed (after passing the shock wave) by the supersonic relaxation zone. Parameter is the background pressure (20, 100 and 200 Pa). The dashed curves and the points represent the measurements. The full curves correspond to the calculated profiles.

After the shock the plasma expands towards the substrate holder. Quasi–one–dimensional model calculations are employed again. This approximation is probably the least valid for the description of the shock, which is described by the Rankine–Hugoniot equations. The shock will be three–dimensional; also the measurements average over quite a long distance as shown in Fig. 4. The agreement is still reasonable as is shown in Fig. 11. Clearly, the shock is observed less sharp than follows from the one–dimensional model. In Fig. 12 a three–dimensional plot is given of the axial velocity. Together with the measured lateral profiles of the electron density shown in Fig. 13, a total electron fluence can be calculated. Calculations show that the main ions are hydrogen and carbon ions if sufficient CH_4 is added to the argon flow.

Finally, some remarks on the deposition rate and the quality of the layer will be made. In Fig. 14 the deposition rate is shown as a function of the carbon flux, both for C_2H_2 and CH_4. It can be observed that the deposition rate increases with the carbon flux; only for CH_4 a saturation is observed. This difference between C_2H_2 and CH_4 is thought to be due to the difference in energy per carbon ion, which has to be in the argon flux to ionize the carbon.

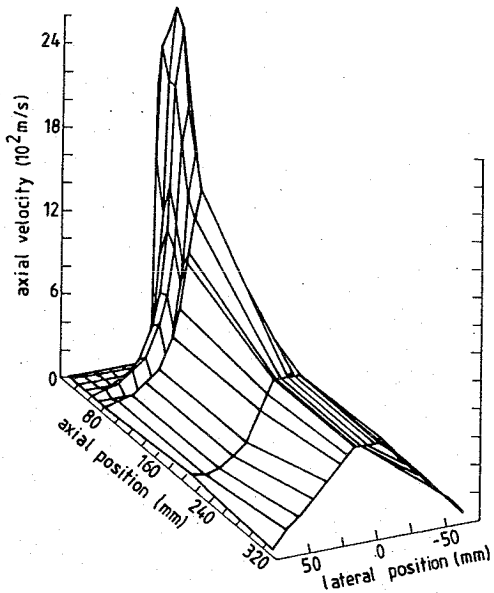

Figure 12. Three–dimensional view of the spatial profile of the plasma velocity in the expansion of the arc plasma into the vacuum system.

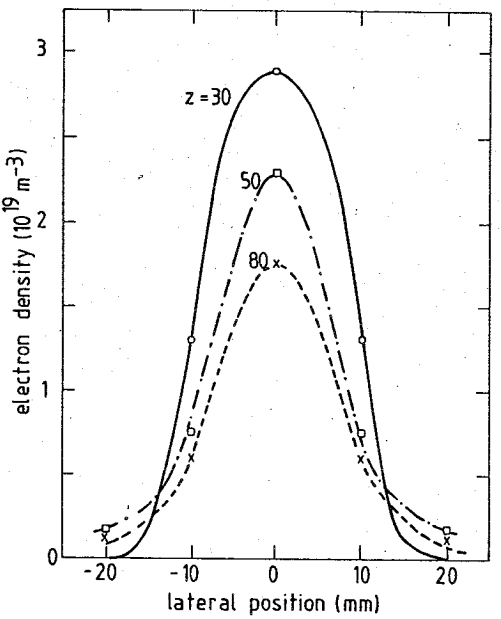

Figure 13. The measured lateral profiles of the electron density at three axial positions (30, 50 and 80 mm).

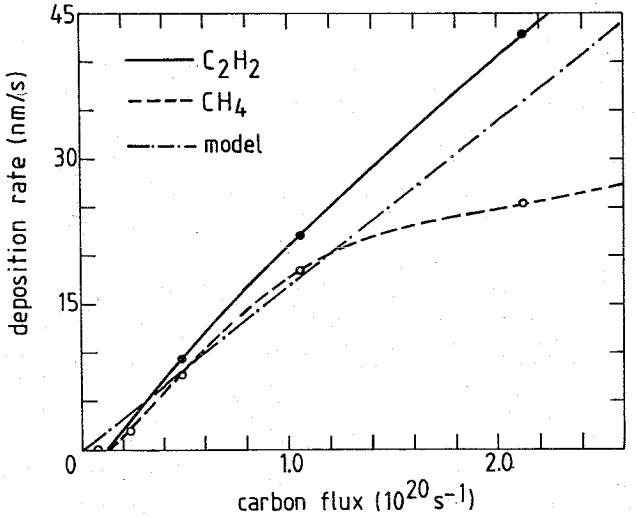

Figure 14. The deposition rate as a function of the injected number of carbon atoms for an argon plasma with an admixture of methane (CH_4) or acetylene (C_2H_2). The dash–dotted curve represents the calculated values.

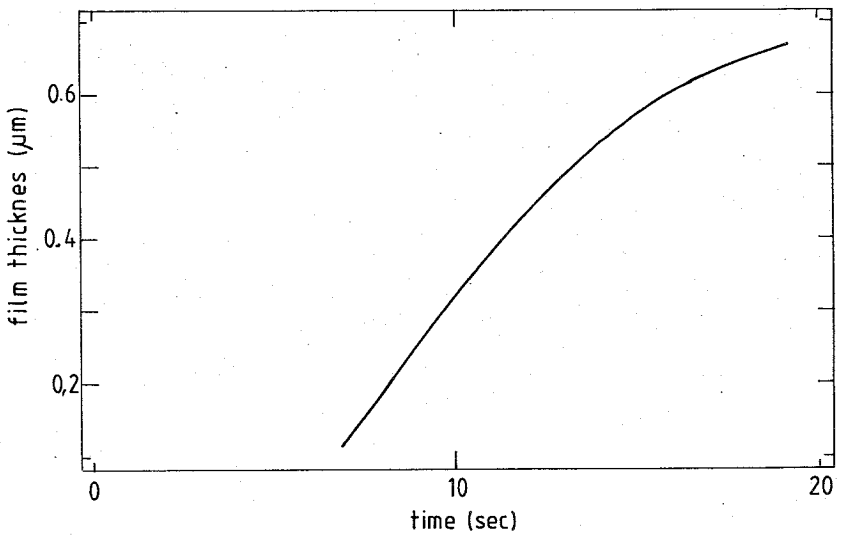

Figure 15. Film thickness as a function of time.

The film thickness grows linear in time until the substrate temperature rises and the deposition rate declines (see Fig. 15). It proves that substrate temperature is an important parameter.

Finally, the refractive index at $\lambda = 632.8$ nm, measured with the He–Ne ellipsometer and the bandgap, determined by the spectroscopic ellipsometer, are shown in Figs. 16a and 16b. Both are plotted against the so–called energy coefficient Q. The latter is defined as the ratio of the carbon flux and the product of the argon flux times the arc power in W. So the energy coefficient Q can be interpreted as a measure for the reciprocal value of the energy available to every incorporated carbon atom or ion. From Fig. 17 it can be concluded that also the hardness is a function of the energy coefficient.

5. CONCLUSION

It can be concluded that this new approach to plasma deposition, which in some way in methodology is similar to low pressure plasma spraying, is very effective and could be a good alternative for producing high quality layers.

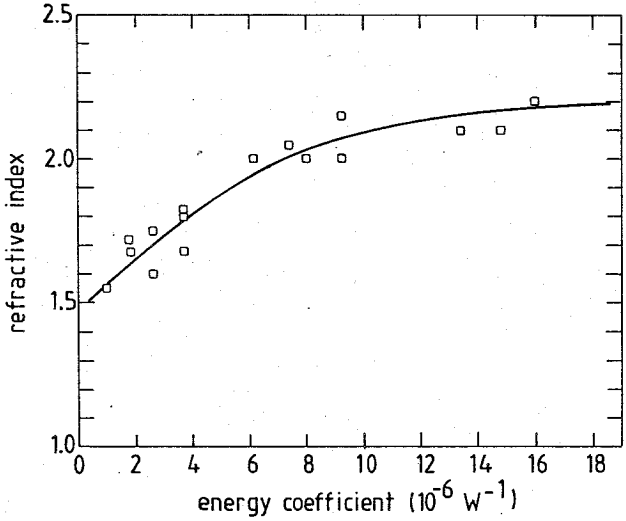

Figure 16a. All measurements using the *in–situ* ellipsometer accumulated in a plot of the refractive index versus the energy coefficient Q, defined as the ratio of the carbon flux and the power product P (argon flux in scc/s times arc power in W).

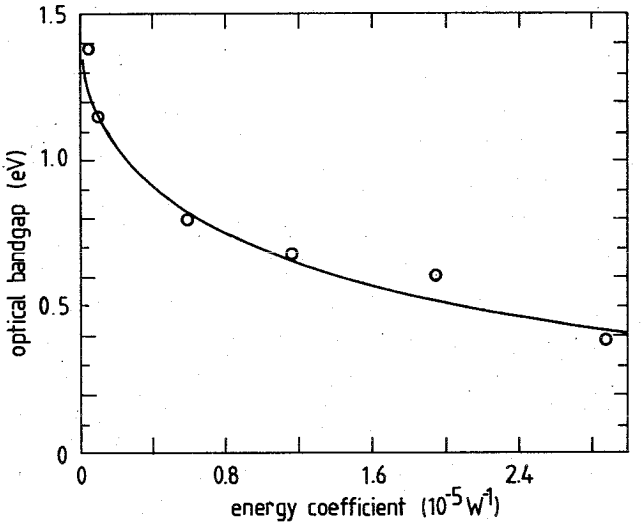

Figure 16b. The optical bandgap as determined with the spectroscopic ellipsometer as a function of the energy coefficient Q.

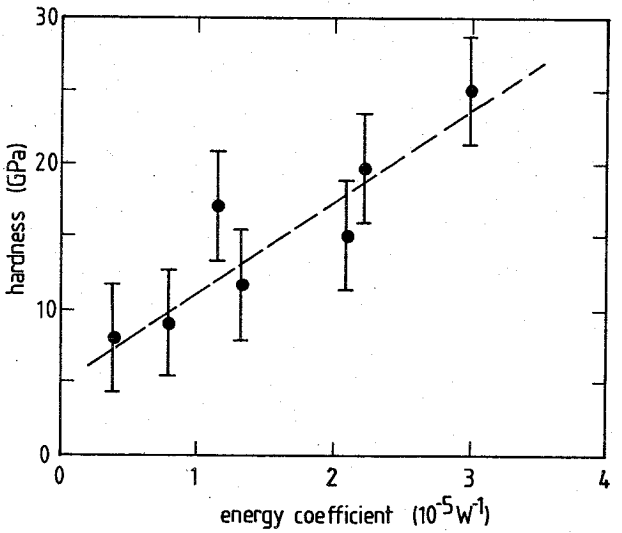

Figure 17. Hardness of the deposited films as a function of the energy coefficient Q. The experimental values are obtained with scratch tests.

ACKNOWLEDGEMENTS

The authors would like to thank M.J.F. van de Sande for his technical assistance. The investigations in the program of the Foundation for Fundamental Research of Matter (FOM) have been supported by the Netherlands Technology Foundation (STW).

REFERENCES

[1] Schram, D.C., Bisschops, T.H.J., Kroesen, G.M.W. and De Hoog, F.J. (1987). Plasma surface modification and plasma chemistry. Plasma Phys. Contr. Fus. 29, 1353–1364.
[2] Maecker, H. (1956). Z. Naturforschung 11a, 457.
[3] De Haas, J.C.M. (1987). Private communication, Eindhoven University of Technology, Eindhoven, The Netherlands.
[4] Kroesen, G.M.W. (1988). "Plasma deposition: Investigations on a new approach". Ph.D. Thesis, Eindhoven University of Technology, Eindhoven, The Netherlands, 1–103.
[5] Van der Sijde, B., Van der Mullen, J.J.A.M. and Schram, D.C. (1984). Collisional radiative models in plasmas. Beitr. Plasmaphys. 24, 447–473.
[6] Kroesen, G.M.W. (1983). Internal Report VDF/NT 83–07 (in Dutch), Eindhoven University of Technology, Eindhoven, The Netherlands.
[7] Van der Mullen, J.J.A.M., Nowak, S., Van Lammeren, A.C.A.P., Schram, D.C. and Van der Sijde, B. (1988). Non equilibrium characterization and spectroscopic analysis of an inductively coupled argon plasma. Spectrochim. Acta 43B, 317–324.
[8] Azzam, R.M.A. and Bashava, N.M. (1968). "Ellipsometry and polarized light". North Holland Publ. Comp., Amsterdam, The Netherlands.
[9] Kroesen, G.M.W., Schram, D.C. and De Haas, J.C.M. (1988). Submitted for publication in J. Appl. Phys.
[10] Kroesen, G.M.W., Schram, D.C., Wilbers, A.T.M. and Meeusen, G.J. (1988). Submitted for publication in AIAA.
[11] Vargaftik, N.B. (1975). "Table on the thermophysical properties of liquids and gases". Hemisphere Publ. Comp. (Wiley), Washington, USA.